Indian J Phys
https://doi.org/10.1007/s12648-026-04093-6

ORIGINAL PAPER

Impacts of substitutional Mn-doping on the structural, morphological, optical, and photocatalytic properties of MoS_2 nanoparticles synthesized by hydrothermal method

M A M Hussien[1,2]* and A Abu El-Fadl[1,2]

[1]Physics Department, Faculty of Science, Assiut University, Assiut 71516, Egypt

[2]Lab. of Smart Materials for Energy Futures, Physics Department, Faculty of Science, Assiut University, Assiut 71516, Egypt

Received: 27 January 2026 / Accepted: 02 June 2026

Abstract: In this article, pure and manganese (Mn)-substituted molybdenum disulfide ($Mo_{1-x}Mn_xS_2$) nanostructures were synthesized using the hydrothermal method for photocatalytic activity. A number of characterization techniques were employed to examine the impact of Mn incorporation on the morphological, structural, optical, and photocatalytic characteristics of MoS_2. The samples were analyzed using field emission scanning electron microscopy, which revealed an aggregated nanoflower-like structure in the recorded images. X-ray diffraction technique was performed to examine the crystal structure of pure and Mn-doped MoS_2 samples, and the results confirmed the formation of the 2H-MoS_2 polytype in all the as-prepared nanostructures, with a reduction in the average crystallite size by increasing the dopant concentration. Edge-terminated active sites in the Mn-doped samples were indicated by Raman analysis. Also, further investigation of the structure was carried out using Fourier transform infrared spectroscopy, confirming the presence of the characteristic Mo-S band. The elemental composition of pure and Mn-doped MoS_2 nanoflowers (NFs) was verified by energy-dispersive X-ray spectroscopy. Brunaure-Emmett-Teller surface analysis was performed to find out the impact of Mn doping on the surface area. The optical properties were observed through ultraviolet–visible spectroscopy, demonstrating allowed direct transitions with an optical energy bandgap that gradually decreased with increasing Mn concentration. The photocatalytic performance of undoped and Mn-doped MoS_2 NFs was evaluated through the degradation of methylene blue (MB) dye under visible-light irradiation. This study demonstrates that high photocatalytic efficiency (96% MB degradation in 60 min under visible light) is achieved at a low Mn concentration (1.5%), highlighting that controlled Mn incorporation enhances charge separation without excessive doping.

Keywords: MoS_2; Mn-doped MoS_2; $Mo_{1-x}Mn_xS_2$ nanostructure; Methylene blue; Photocatalysis; Degradation

1. Introduction

In the last century, the rapid growth of industry led to significant economic prosperity, which facilitated life for human beings and made it more accessible. However, from another point of view, this growth led to a rise in the level of pollutants, which severely harms the ecosystem. For example, several industries, such as those producing textiles, paper, plastics, and cosmetics, release large amounts of wastewater containing organic dyes and pollutants into water sources. Most of these pollutants are extremely toxic and, therefore, cannot be easily degraded naturally [1]. Even trace amounts of organic pollutants and dyes discharged into water streams can affect humans and living organisms in a very dangerous manner. Therefore, it has become essential to degrade organic pollutants and toxic dyes from their sources before they arrive the water drains. In this context, developing a stable, effective, and inexpensive method to wastewater treatment is very important. Compared with various methods for removing organic dyes, photocatalytic degradation is considered a sustainable, environmentally friendly, and low-cost solution [2, 3]. Titanium dioxide (TiO_2) and zinc oxide (ZnO) have been widely used as photocatalysts, and they are thought to have outstanding photocatalytic activity against different dyes and have been extensively researched [4–6]. However, because of their relatively large energy bandgap, their

*Corresponding author, E-mail: physicistmahmoud@aun.edu.eg

Published online: 19 June 2026

practical application is limited and confined to the ultraviolet region (4–5% of natural light) [7–10]. Thus, the aim of this research is to develop new and efficient materials that can effectively utilize the visible part of the electromagnetic spectrum to degrade organic pollutants.

Visible-light-activated photocatalysts have attracted significant research attention due to their remarkable abilities in energy generation and environmental applications. Nanostructures engineered to be responsive to visible light have been proven to capture light effectively [11–13]. For innovative and advanced applications, visible-light-driven photocatalytic materials are crucial, as they must absorb a substantial portion of the sunlight's visible spectrum [14]. Since Fujishima's remarkable breakthrough in water splitting in 1972, semiconductor-based photocatalysts have emerged as one of the most promising approaches for degrading organic pollutants through light illumination [15]. But the low surface area and inadequate light absorption of these semiconductor-based photocatalysts restrict their overall performance and ability to achieve high efficiency. 2D transition metal dichalcogenides (TMDCs) have attracted considerable attention as photocatalysts in recent years due to their large surface-to-volume ratios, porous structures that increase the number of active catalytic sites, and an adjustable bandgap that facilitates the movement of charges [16]. Their unique optical and electronic characteristics are due to their fundamental layered structure. MX_2 is the general formula for TMDs, where M is a transition metal element from group IV (Ti, Zr, or Hf), group V (V, Nb, or Ta), or group VI (Mo or W) in the periodic table, and X is a chalcogen element from group VI (S, Se, or Te) [17, 18]. M is attached to X via weak Van der Waals force [19, 20].

Among the aforementioned materials, MoS_2, which has been extensively explored as a visible-light photocatalyst, is considered to be a superior member of TMDCs due to its layered crystal structure, similar to that of graphene, and it is also an abundant and cost-effective semiconducting substance [21–23]. It is made up of layers arranged in a trigonal prismatic pattern with one atomic plane of molybdenum (Mo) sandwiched between two atomic planes of sulfur (S) [24]. Each Mo and S atom is attached to each other via a strong covalent bond, while the layers themselves are linked to each other by weak Van der Waals forces [25]. According to the variance of the atomic stacking order and atomic coordination, there are three recognized polytypes of MoS_2: 1T, 2H, and 3R. The 1T phase has tetragonal symmetry containing one S-Mo-S layer for each cell with octahedral coordination of Mo and S atoms; it exhibits metallic behavior with space group P3m1, where T refers to the trigonal structure. The 2H-MoS_2 polytype (space group: P63/mmc) has two layers of S-Mo-S per unit cell, where each Mo atom is surrounded by six S atoms in a trigonal prismatic shape; H here refers to the hexagonal structure. The 3R phase corresponds to rhombohedral symmetry consisting of three S-Mo-S layers per unit cell and displays trigonal prismatic coordination; R here refers to the rhombohedral structure. The 2H polytype is the most stable and has semiconducting properties, while the 1 T and 3R polytypes are less stable [26]. Figure 1a shows the three-dimensional illustration of the layered MoS_2 structure, and the three MoS_2 polytypes are presented in Fig. 1b as designed using VESTA software [27, 28].

Bulk MoS_2 is classified as an n-type semiconductor with an indirect bandgap of approximately 1.2 eV, which is unsuitable for activating the photocatalytic process and separating charge carriers [29]. However, because the number of MoS_2 layers has a substantial effect on its optoelectronic characteristics [30], previous reports indicate that layered MoS_2 has a direct optical bandgap of around 1.9 eV, high mobility of charge carriers, and excellent absorbance in the visible-light zone, which makes it suitable for photocatalysis [31, 32]. In spite of these advantages, the use of MoS_2 as a photocatalyst is still restricted because charge carrier recombination occurs quickly and the number of active edge sites is limited [33]. According to previous research, the photocatalytic activity of MoS_2 strongly depends on its edge sites [22]. Hence, many strategies have been suggested to increase the number of edge sites and, therefore, boost the photocatalytic activity of MoS_2 [34]. Some of these strategies include chemical doping or modification, incorporation with other traditional photocatalysts, forming heterostructures with other semiconductors, and so on. For example, some previous studies used MoS_2/TiO_2 [35, 36], MoS_2/ZnO [37, 38], $MoS_2/FeZnO$ [39], MoS_2/WO_3 [40], and MoS_2-RGO/ZnO as photocatalyst heterostructures for MB dye degradation [41]. However, there are limited publications on doping with transition metal ions in semiconducting p-type MoS_2 to remove organic pollutants, such as Ni–MoS_2 [42], Ag–MoS_2 [43], Cd–MoS_2 [44], and Mn–MoS_2 [45]. According to these studies, adding metal atoms can create more sites that are active for catalysis, thereby enhancing the photocatalytic performance.

Experimentally, MoS_2 can be manufactured via various techniques such as RF magnetron sputtering [46], chemical vapor deposition [47], spin coating [48], ultrasonic spray pyrolysis [49], sol–gel [50], sulfurization [51], decomposition of ammonium tetrathiomolybdate [52], and hydrothermal method [53, 54]. The hydrothermal technique is highly advantageous to conventional and non-conventional synthesis techniques because of its inexpensive cost, simplicity, and fewer precursor materials [55]. Through the hydrothermal method, specimens are directly collected from the solution, resulting in a regular and

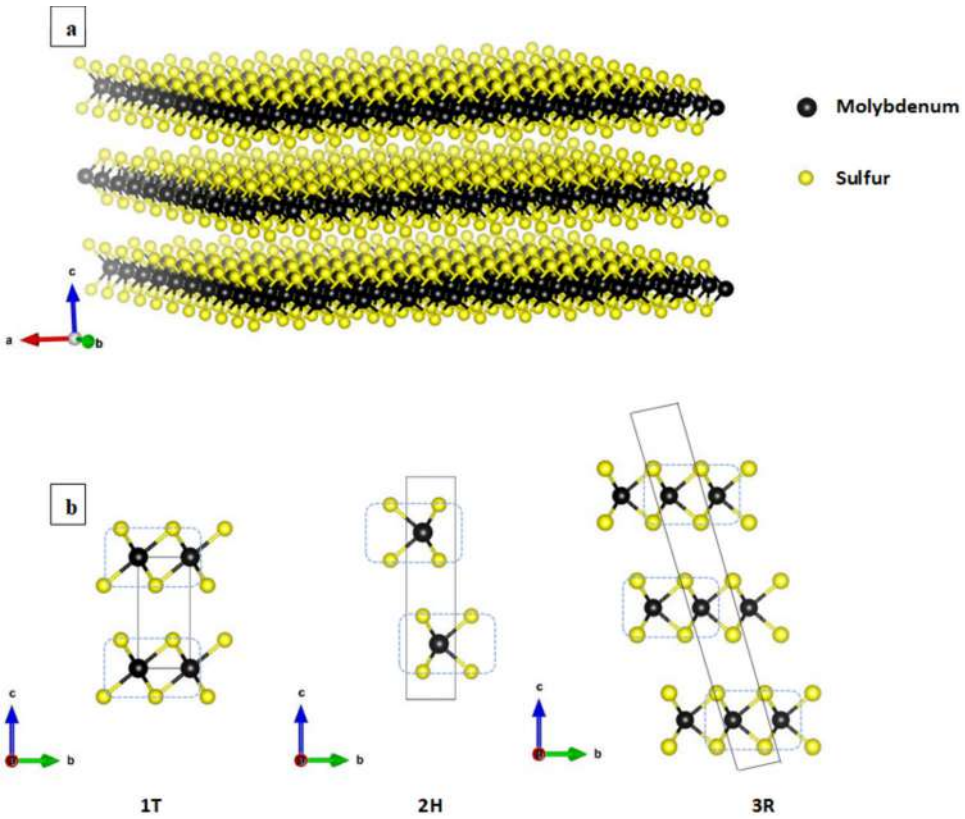

Fig. 1 **(a)** Schematic representation of layered MoS_2, **(b)** different MoS_2 polytypes

uniform rate of nucleation, nanoparticle size, and morphology without requiring high temperatures or complex procedures [56, 57].

Manganese (Mn) is one of the transition metal dopants that are best suited for substitutional incorporation into the MoS_2 lattice because of its ionic radius ($Mn^{2+} \approx$ 0.08 nm), which is similar to that of Mo^{2+} ($\approx$ 0.079 nm) [58]. This allows for lattice substitution with minimal structural disruption while also causing controlled lattice distortion and defect formation. The density of catalytically active centers is known to be increased by such substitution, thereby produces more active edge sites and raises the concentration of sulfur vacancies [59, 60]. From an electrical point of view, adding Mn can modify the electronic properties of MoS_2, making it behave more like a semimetal, which makes it easier for charge carriers to transport by introducing localized impurity states into the band structure [61]. Mn is an effective electron-trapping center, which means it slows down the fast recombination of electron–hole pairs that are photogenerated and makes charge separation much more efficient [59, 62]. Multiple oxidation states (Mn^{3+}/Mn^{4+}), which facilitate interfacial charge transfer between the Mn sites and the MoS_2 lattice, are often associated with this trapping phenomenon [59, 60]. Mn doping has a significant effect on the optical properties of MoS_2 [59, 62] because it makes the bandgap narrower and creates defect-related energy states that extend optical absorption into the visible range. These defect states improve the ability to harvest solar light and enable the absorption of photons with energies below the bandgap. Both of these effects are important for photocatalytic applications. It has also been noted that Mn incorporation increases the exposed surface area, porosity, and surface roughness, all of which help reactant molecules stick to the surface and speed up the photocatalytic reaction [60, 63]. Mn doping is a highly effective strategy to improve the photocatalytic performance of MoS_2-based systems because it combines defect engineering, band structure manipulation, enhanced visible-light absorption and improved charge carrier separation.

Previous studies on Mn-doped MoS_2 photocatalysts have demonstrated that performance is highly dependent on dopant concentration, irradiation conditions, and reaction time. For instance, a relatively high Mn loading (20%) achieved complete degradation of MB within 90 min under a low-power 25 W lamp [59], while another study using 3% Mn-doped MoS_2 required a prolonged irradiation time of 240 min to reach only 40.9% degradation of rhodamine B dye under compact light illumination [58]. Although higher efficiency (91%) was reported for 3% Mn-doped MoS_2 within 55 min, this was achieved under a high-

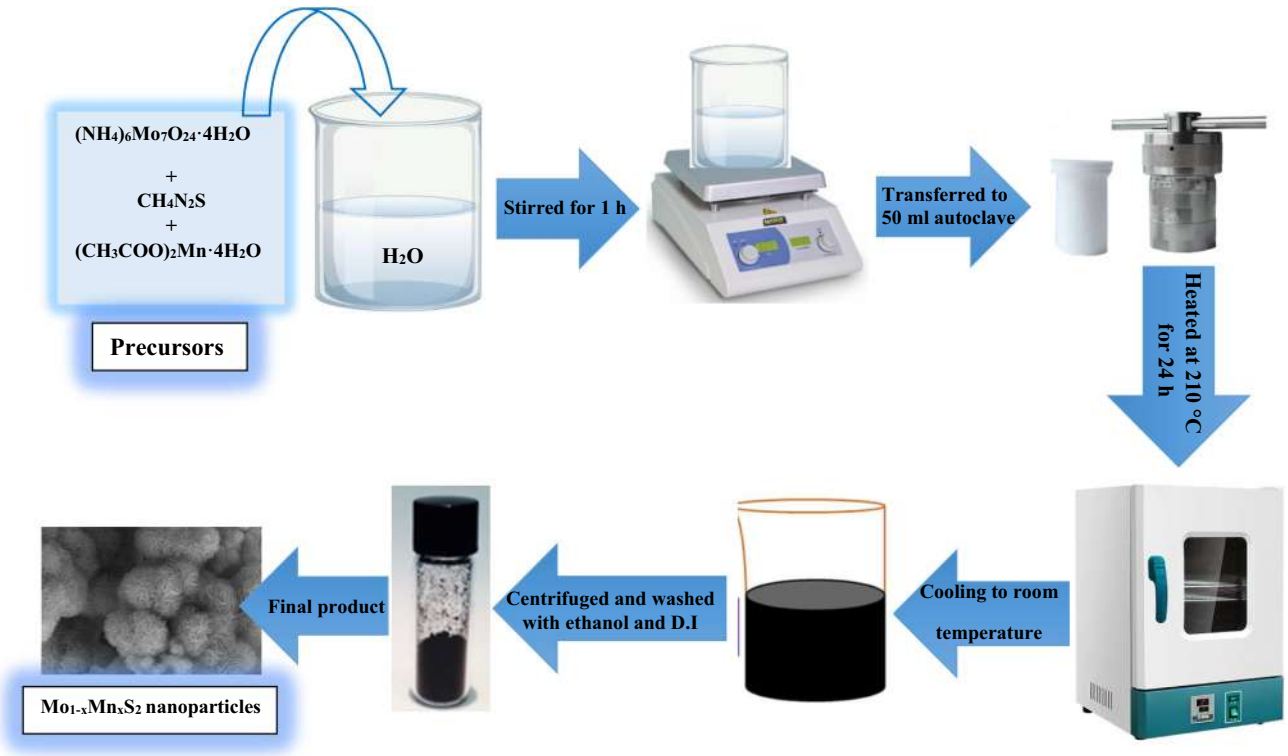

Fig. 2 Diagrammatic representation of the preparation procedure of $Mo_{1-x}Mn_xS_2$ nanoparticles

intensity 150 W Hg lamp [45], indicating the strong influence of irradiation conditions.

Here, we report the preparation of both undoped and Mn-doped MoS_2 nanoparticles ($Mo_{1-x}Mn_xS_2$) with different Mn concentrations (x = 0.005, x = 0.01, and x = 0.015) by a facile and cost-effective one-step hydrothermal method to investigate their photocatalytic activity for MB under visible light irradiation. The present work demonstrates that a significantly lower Mn doping concentration (1.5%) can achieve a high photocatalytic efficiency of 96% MB degradation within 60 min under visible light irradiation using a moderate 150 W halogen lamp. This result highlights that optimized low-level Mn incorporation is sufficient to achieve superior performance without relying on excessive dopant concentration or high-intensity irradiation conditions.

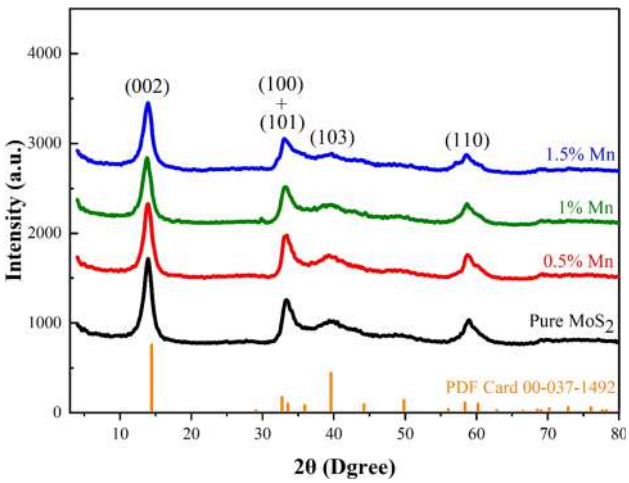

Fig. 3 XRD patterns with indexed peaks of the hydrothermally synthesized $Mo_{1-x}Mn_xS_2$ NFs

2. Experimental details

2.1. Materials

Ammonium molybdate tetrahydrate ($(NH_4)_6Mo_7O_{24}·4H_2O$), manganese (II) acetate tetrahydrate ($(CH_3COO)_2Mn·4H_2O$), thiourea (CH_4N_2S), ethyl alcohol (CH_3CH_2OH), methylene blue dye ($C_{16}H_{18}ClN_3S$), and distilled water. All of these chemicals were purchased from the ALPHA CHEMIKA company with extra purity (99.9%) without any further purification.

2.2. Hydrothermal preparation of pure and Mn-doped MoS_2 nanoparticles

Pure MoS_2 nanoparticles were synthesized via the hydrothermal method. Briefly, 1.24 g of ammonium molybdate tetrahydrate and 1.645 g of thiourea were mixed

with 35 mL of distilled water and stirred for 1 h to obtain a clear solution. The mixture was transferred into a 40-mL Teflon-lined autoclave and heated to 210 °C for 24 h. The autoclave was then cooled naturally to room temperature, and the black precipitate was separated by centrifugation at 3000 rounds per minute and washed several times with distilled water and ethyl alcohol before being ground to produce pure MoS_2 nanoparticles. $Mo_{1-x}Mn_xS_2$ ($0.005 \leq x \leq 0.015$) nanoparticles were prepared following the same procedure used to synthesize pure MoS_2 by using $(CH_3COO)_2Mn{\cdot}4H_2O$ as the precursor of Mn with stoichiometric weight ratios in the reaction. Figure 2 illustrates the schematic representation of the $Mo_{1-x}Mn_xS_2$ nanostructure synthesis process, and the following chemical reactions (Eqs. 1, 2, and 3) illustrate the reactions that occurred through the synthesis process to get pure MoS_2 nanoparticles [64].

$$CH_4N_2S + 2H_2O \rightarrow CO_2 \uparrow + 2NH_3 \uparrow + H_2S \quad (1)$$

$$(NH_4)_6Mo_7O_{24}4H_2O + 28H_2S + 8NH_3 \rightarrow 7(NH_4)_2MoS_4 + 28H_2O \quad (2)$$

$$5O_2 + 2N_2 + 2C_6H_8O_7 + 2(NH_4)_2MoS_4 \rightarrow 2MoS_2 + 12CO_2 + 4(NH_4)_2S \quad (3)$$

2.3. Degradation experiment

The photocatalytic activities of pure and Mn-doped ($Mo_{1-x}Mn_xS_2$) NFs were evaluated through the degradation of MB dye in an aqueous solution under visible light irradiation (150 W halogen lamp). In a typical experiment, 10 mg of the catalyst was added to a 100 mL MB solution at a concentration of 10^{-5} M under continuous stirring at room temperature. To achieve the adsorption–desorption equilibrium of MB molecules on the photocatalyst surface, the solution was agitated in the dark for 1 h prior to the irradiation process. At regular time intervals, 3 mL of the solution was collected and centrifuged to eliminate the catalyst, and the residual concentration of MB was measured using a UV–Vis spectrophotometer in the wavelength range of 400–700 nm.

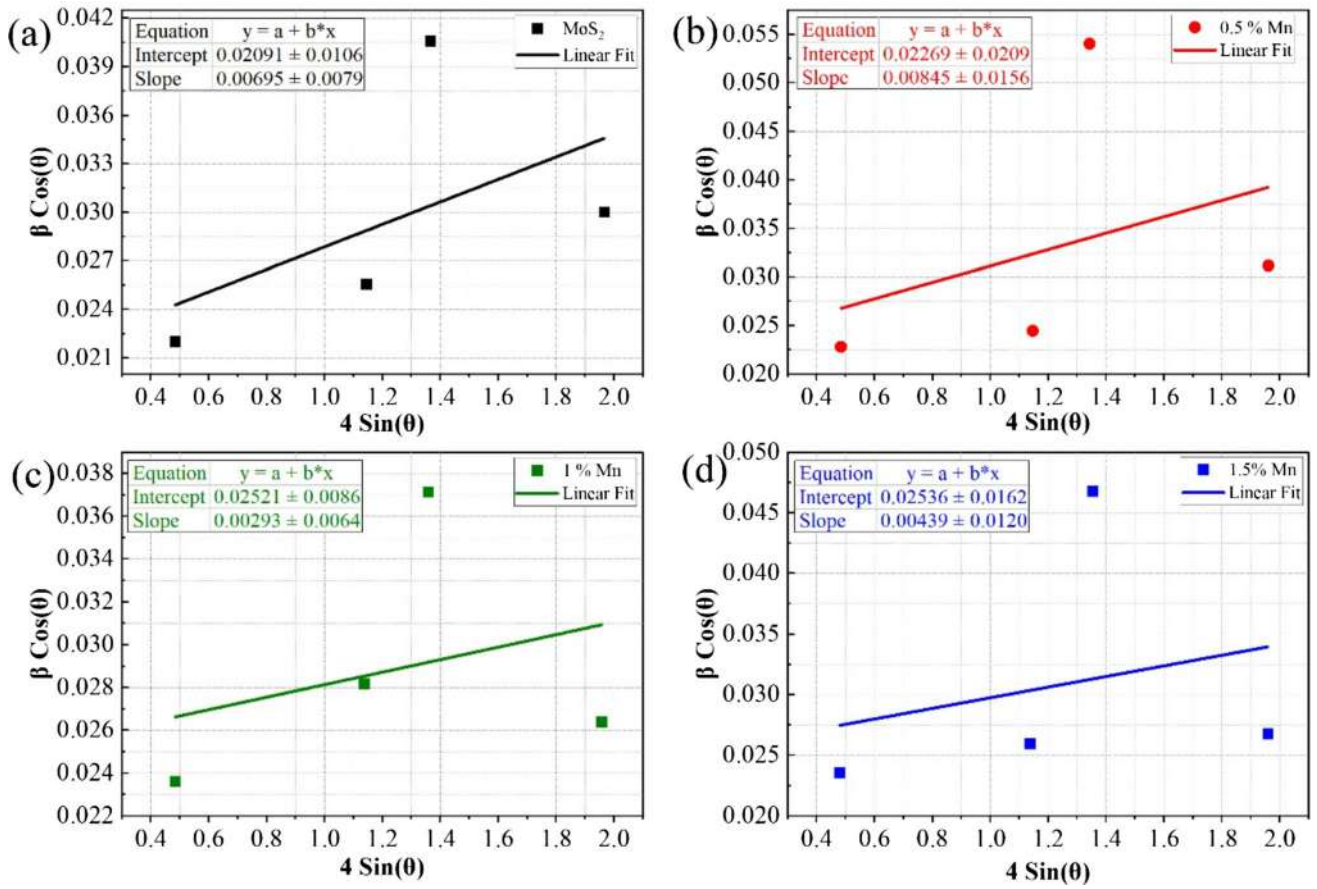

Fig. 4 Calculated W–H plots of **(a)** pure, **(b)** 0.5%, **(c)** 1%, and **(d)** 1.5% Mn-doped MoS_2 NFs

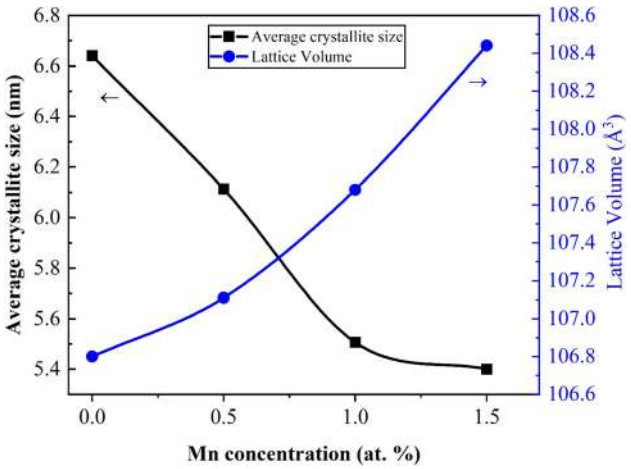

Fig. 5 Change of the average crystallite size (D_{XRD}) and lattice volume (V) with Mn concentration for $Mo_{1-x}Mn_xS_2$ NFs

3. Characterization methods

The crystalline phase and the structural properties of the as-prepared photocatalysts were examined through a Philips X-ray diffractometer (model PW 1710, Holland), employing Cu–K_α radiation (λ = 0.15405 nm) at an applied voltage of 40 kV and a current of 0.03 A. The vibrational and bonding properties of pure and Mn-doped MoS_2 samples were evaluated using a Raman spectrometer (Jobin–Yvon LabRam HR80). FESEM (ZEISS Sigma 500 VP) was used to examine the morphology of the prepared catalysts. FTIR analysis of the synthesized samples was conducted utilizing the NICOLET FTIR 6700 spectrometer through the use of the KBr pellet technique across the wavenumber range of 400–4000 cm^{-1}. An energy dispersive spectrometer (Model ULTRADRY QUANTA Field Emission Gun 250) connected to a scanning electron microscope unit was utilized to find out the elemental composition of the prepared samples. The analysis of the specific surface area was conducted through a Quantachrome surface area/pore size analyzer (NOVA 3200e) based on the BET method. Prior to the measurements, the samples were degassed under vacuum at 250 °C for 120 min. Subsequently, nitrogen adsorption–desorption isotherms were recorded at −196 °C. Computerized JASCO V-770 UV–Vis-NIR spectrophotometer was used to record the absorbance of the as-synthesized pristine and Mn-doped MoS_2 nanostructures within a range of 300–800 nm.

4. Results and discussion

4.1. X-ray diffraction

Powder XRD analysis was performed to investigate the crystal structure of the as-prepared $Mo_{1-x}Mn_xS_2$ ($0 \leq x \leq 0.015$) nanoparticles. All samples of pure and Mn-doped MoS_2 reveal a single hexagonal 2H-MoS_2 phase with space group P63/mmc as indexed in JCPDS file no. 37–1492. This is evident in Fig. 3, where the prominent diffraction peaks detected at 2θ = 13.9°, 32.6°, 33.5°, 39.46°, and 58.50° correspond to (002), (100), (101), (103), and (110) crystallographic planes, respectively [65]. The (002) plane, which has the lowest energy surface, showed the main peak of pure MoS_2, indicating that the S–Mo–S layers are well stacked along the c axis [66, 67]. All Mn-doped samples exhibited diffraction patterns similar to that of pure MoS_2 without the appearance of secondary impurity phases such as MnO_2, Mn_2O_3, Mn_3O_4, Mo_2O_3, or MoO_3. This observation confirms the successful incorporation of Mn ions into the MoS_2 lattice without altering the hexagonal crystal structure and indicates that the Mn concentration remains within the solubility limit and that the doped samples are formed in a polycrystalline single phase. Mn ions can diffuse into the Mo ion matrix to occupy the lattice sites without altering the hexagonal phase due to the comparable structures of Mn and Mo atoms [68]. The variation in the broadening (FWHM) of the reflected peaks, which ranging from 1.26° to 3.28° across various hkl reflections, can be explained by the existence of tiny grains compared to others [68]. In addition, it is noted from the diffraction pattern that the intensity of the diffraction peaks slightly decreases by increasing the doping ratio, implying that the crystallinity of the Mn-doped samples is reduced by increasing the Mn concentration in the MoS_2 lattice [45].

To further comprehend how Mn ions affect the lattice characteristics of undoped MoS_2, the microstructural properties of the $Mo_{1-x}Mn_xS_2$ ($0 \leq x \leq 0.015$) were examined using the Williamson-Hall (W–H) model represented in Eq. (4). This model was employed to estimate the average crystallite size (D) and the nanocrystals' micro strain (ε) [69]. In order to do that, Eq. (5) must be used to remove the instrumental broadening from the X-ray diffraction peak pattern, which consists of the instrumental broadening and crystallite size broadening. Hence, the whole broadening caused by strain and size for a specific peak that had a hkl value can be defined by Eq. (6) [69]. It is worth mentioning here that Eq. (4) is a straight-line relation called the uniform deformation model (UDM) [69]. By plotting 4 sinθ on the X-axis and β_{hkl} cosθ on the Y-axis, the intrinsic strain and the average crystallite size were determined from the slope and the intercept of this line, respectively, as shown in Fig. 4a–d.

$$\beta_{hkl}\cos\theta = \frac{k_s\lambda}{D} + 4\varepsilon\sin\theta \quad (4)$$

$$\beta^2_{measured} = \beta^2_{size} + \beta^2_{instrumental} \quad (5)$$

$$\beta_{hkl} = \beta_{size} + \beta_{strain} \quad (6)$$

where β is the full-width at half maximum of the diffracted peak measured in radians, k_s is the shape factor assigned to be 0.94, λ is the wavelength of Cu K_α radiation measured in nm, and θ is Bragg's angle in radians.

Obviously, as shown in Fig. 5, the average crystallite size gradually decreased with increasing Mn concentration whereas the lattice volume exhibited a slight increase, although the same preparation steps were followed during the synthesis process. Thus, the crystallite size decreased as a result of Mn ions being swapped by Mo ions. According to measurements, the samples' average crystallite size was between 5 and 7 nm. The slight expansion in the lattice volume can be explained by the difference in ionic radii between Mo^{+4} and Mn^{+3} ions, as the ionic radius of Mn^{+3} (0.072 nm) ion is larger than that of Mo^{+4} (0.065 nm).

The lattice parameters (a and c) and the unit cell volume (V) for all the prepared samples starting from x = 0 (pure MoS_2) to x = 0.015 (1.5% Mn-doped MoS_2) were computed using CellRef software [70]. Equations (7) and (8) were also used to calculate the dislocation density (δ) and theoretical density (ρ), respectively [71].

$$\delta = \frac{1}{D^2} \quad (7)$$

$$\rho = \frac{ZM}{N_a V} \quad (8)$$

where Z is the number of molecules per unit cell (Z = 2 for MoS_2), M is the molecular weight, and N_a is Avogadro's number. All the calculated structural parameters are summarized in Table 1.

4.2. Raman spectroscopy

Figure 6 shows the Raman spectra of pure and Mn-doped MoS_2 samples recorded using a 532 nm excitation laser. The main characteristic peaks for the pure sample that matched the E^1_{2g} and A_{1g} vibrational modes were at 379.71 cm^{-1} and 405.78 cm^{-1}, respectively, confirming the 2H-MoS_2 phase. In the E^1_{2g} mode [53, 72], the Mo atom vibrates in the opposite direction and the sulfur atoms vibrate in the same plane. In the A_{1g} vibrational mode [66, 73], only the sulfur atoms vibrate out-of-plane. The longitudinal acoustic mode A_{2u}, is also responsible for the single, lower-intensity peak that was found at 454 cm^{-1} [74]. As the Mn doping percentage increases from 0.5 to 1.5%, the intensities of both the E^1_{2g} and A_{1g} peaks gradually decreased. This behavior is explained by the fact that Mn incorporation into the MoS_2 lattice reduces crystallinity, which is in line with XRD findings.

In addition to the MoS_2 peaks, Mn-doped samples displayed two additional peaks at 353.3 cm^{-1} and 489 cm^{-1}. These peaks notably became more prominent in 1% and 1.5% Mn-doped samples. These newly observed peaks correspond to the vibration of Mn atoms [75]. This peak becomes more intense as the ratio of Mn increases. The number of exposed edges in MoS_2 nanoparticles is determined by the intensity ratio of the A_{1g} mode to the E^1_{2g} mode [76]. The ratio is observed to be largest for 1.5% Mn-doped MoS_2, indicating a higher density of edge terminated structures [77, 78]. The chance of exposed active sites is increased by these edge-terminated structures, leading to higher catalytic activity [79].

4.3. Morphology and microstructure

The morphological properties of the as-synthesized $Mo_{1-x}Mn_xS_2$ samples were examined using FESEM in order to examine the morphology of pure MoS_2 and detect any morphological changes due to the Mn doping process. As shown in Fig. 7a, pure MoS_2 (x = 0) exhibits a compact hierarchical nanoflower-like structure, and each flower is composed of intertwined MoS_2 closely packed petal-like thin nanosheets. Mn doping did not impact the flower-like nanostructures of MoS_2. This can be clearly observed in Fig. 7b–d, which reveal that the recorded SEM images for x = 0.005, x = 0.01, and x = 0.015 for 0.5%, 1%, and 1.5% Mn-doped MoS_2, respectively. The absence of significant morphological changes may be attributed to the relatively low Mn doping concentrations employed in the

Table 1 Calculated structural parameters of pure and $Mo_{1-x}Mn_xS_2$ nanoflowers obtained from XRD analysis

X	a (Å)	c (Å)	V (Å^3)	ρ (gm/cm^3)	D_{XRD} (nm)	ε × 10^{-3}	δ × 10^{-3} (nm^2)
0	3.137	12.53	106.80	4.978	6.64	7	22.68
0.005	3.141	12.54	107.11	4.938	6.11	8.4	26.76
0.01	3.150	12.54	107.68	4.869	5.51	2.9	32.97
0.015	3.152	12.60	108.44	4.793	5.46	4.4	33.50

present study [58]. Sasi and his colleagues [45] reported in their study that the morphology of the as-synthesized pristine and Mn-doped MoS_2 (up to 3% Mn) is composed of thin sheets that have a petal-like shape and a close packing aggregate to form structures that are hierarchical flower-like, indicating that the Mn doping had no effect on the flower-like nanostructures of MoS_2.

The lack of influence on the morphology of MoS_2 upon Mn doping was not limited only to the Mn element as a dopant; other previous research confirmed the preservation of the characteristic MoS_2 morphology by adding some other transition metal elements such as Ni, Co, and Cu. For example, Mosconi et al. [80] found in their research that similar lamellar morphology is maintained for all the different ratios of Ni-doped MoS_2 (up to 15%) which examined via SEM. Chacko et al. [81] showed in their paper that the as-synthesized and Ni-substituted MoS_2 samples of the $Mo_{1-x}Ni_xS_2$ nano-system ($0.01 \leq x \leq 0.03$) have a 2D hierarchical curly sheet-like architecture (10^{-15} nm thickness) after being studied by FESEM. Lu et al. [82] reported in their work that cobalt-doping did not produce noticeable morphological changes of $Mo_{1-x}Co_xS_2$ compared to pure MoS_2. Similarly, Zhu et al. [83] found that the recorded SEM images exhibited nearly identical morphology between pure MoS_2 and Cu-doped MoS_2.

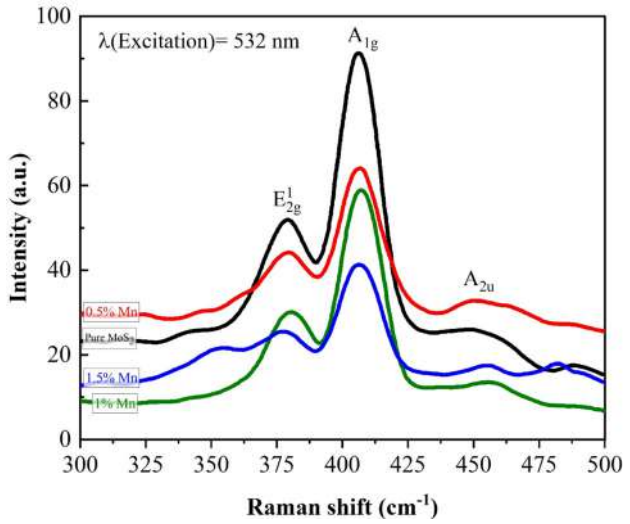

Fig. 6 Raman spectra of $Mo_{1-x}Mn_xS_2$ NFs

4.4. FT–IR spectroscopy

FT-IR analysis is a crucial technique for quickly and efficiently identifying the chemical molecules and functional groups present in the investigated specimen [84, 85]. The FT-IR spectra of $Mo_{1-x}Mn_xS_2$ ($0 \leq x \leq 0.015$) NFs were examined in order to verify the formation of nanostructures as well as to detect any changes that arise because of the doping process. As shown in Fig. 8, the undoped MoS_2 spectrum shows absorption bands centered at 590 cm^{-1}, 750 cm^{-1}, 900 cm^{-1}, 1040 cm^{-1}, 1400 cm^{-1}, 1630 cm^{-1}, 3120 cm^{-1}, and 3440 cm^{-1}. The absorption bands positioned at 590 cm^{-1} and 750 cm^{-1} are credited to Mo–S vibration mode [86, 87]. The band at 900 cm^{-1} corresponds to the S–S bond vibrations [88], and the absorption band at 1040 cm^{-1} is ascribed to the S–O (sulfoxide) asymmetric stretching or C–O stretching bond associated

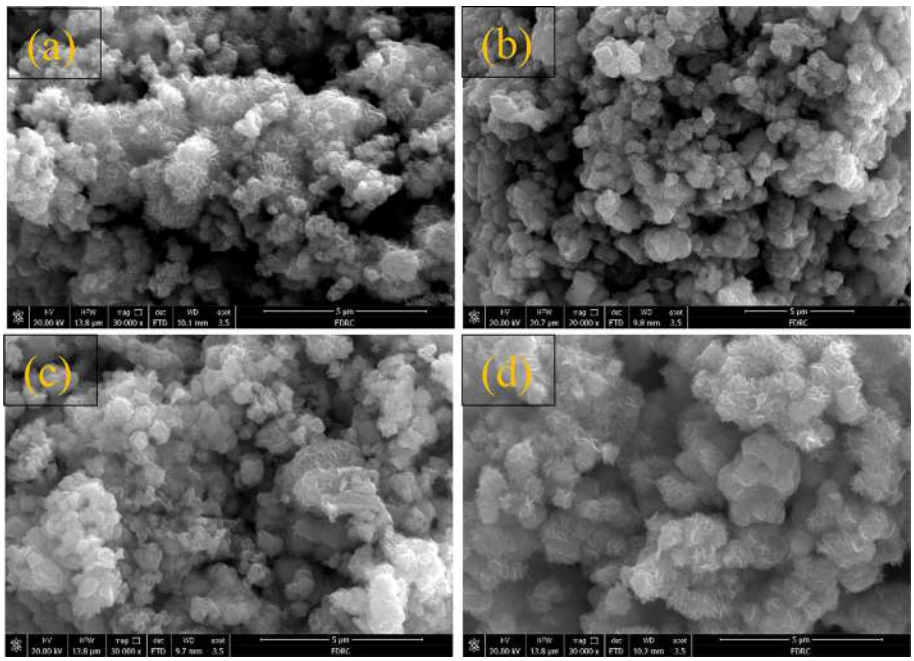

Fig. 7 FESEM images of **(a)** pure, **(b)** 0.5%, **(c)** 1%, and **(d)** 1.5% Mn-doped MoS_2 NFs

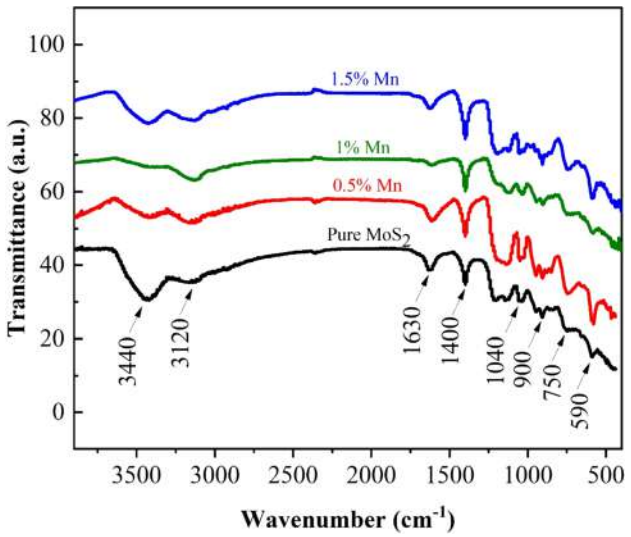

Fig. 8 FTIR spectra of $Mo_{1-x}Mn_xS_2$ NFs

with alcohol groups [89–91]. In addition, the band at 1400 cm^{-1} is due to the S–Mo–S bending vibration peak [92]. The stretching vibrations of O–H groups and the twisting vibration modes of the water molecules on the surface of molybdenum disulfide caused the strong peak at 1630 cm^{-1} and the wide bands at 3120 cm^{-1} and 3430 cm^{-1}, respectively [89, 93]. There are no additional characteristic bands related to the Mn element were appeared in the FTIR spectra of Mn-doped MoS_2 samples due to the relatively low Mn doping concentrations.

4.5. Energy dispersive X-ray spectra

In order to further investigate the chemical composition of the synthesized pure and Mn-doped MoS_2 NFs, the high spatial resolution EDX measurements were conducted. As shown in the EDX spectra of pure MoS_2 (Fig. 9a), distinct peaks corresponding to Mo and S elements were detected, confirming the formation of MoS_2 without the presence of impurity elements. The peaks related to the Mo element are detected at 2470 eV, due to the L_α and L_β characteristic lines, while the S element peak is detected at 2480 eV, indicating the K_α characteristic line [94]. These peaks overlap because the energy levels of S and Mo are so close together [44]. For Mn-doped $Mo_{1-x}Mn_xS_2$ ($0.005 \leq x \leq 0.015$) samples, an additional Mn elemental peak appeared in the spectra (Fig. 9c–d). Furthermore, the quantitative elemental composition analysis presented in Table 2 confirmed that the 0.5%, 1%, and 1.5% Mn-doped samples have a relevant ratio of Mn, confirming that Mn has been successfully incorporated in the MoS_2 lattice.

4.6. Surface area

To study how Mn doping affects the catalyst surface area, N_2 adsorption–desorption isotherms were analyzed for all the prepared $Mo_{1-x}Mn_xS_2$ samples via the Brunaure-Emmett-Teller (BET) surface analysis. Figure 10a and b depict the isotherms for nitrogen adsorption and desorption in both pure MoS_2 and 1.5% Mn-doped MoS_2, respectively. The shape of the isotherm indicates that the photocatalysts exhibit type IV behavior according to the IUPAC classification, characterized by the presence of a hysteresis loop [82]. The pure MoS_2 had a BET surface area of 196,800 $cm^2\ g^{-1}$, while the catalyst doped with 1.5% Mn exhibited a higher surface area of 241,000 $cm^2\ g^{-1}$. These findings demonstrate that incorporating Mn can alter the structure of MoS_2, boost the surface area, and elevate active sites, which improves the photocatalytic activity. The measured values of surface area are collected in Table 3, and these values show a gradual slight increase in the surface area with increasing Mn concentration. This confirms that the samples have a mesoporous quality, as they exhibit the growth of substantial slit-shaped pores.

4.7. UV–Visible spectroscopy

In order to investigate the optical properties of the fabricated undoped and substituted Mn-doped MoS_2, UV–Vis absorption spectra were recorded for the $Mo_{1-x}Mn_xS_2$ ($0 \leq x \leq 0.015$) NFs dispersed in deionized water. The obtained absorption spectra are presented in Fig. 11. Three characteristic absorption bands in the range of 300–700 nm were clearly detected for pristine and Mn-doped samples. The broad band centered in the range of 400–500 nm is due to the direct transition from the depth of the valence band to the conduction band corresponding to C exciton [27, 81, 89]. In addition, two absorption bands with remarkably lower intensity were detected in the visible light range around 600–700 nm, which are the B and A excitonic bands due to direct-gap excitonic transitions from the split valence band to the lowest points of the conduction band at the K point of the Brillouin zone for MoS_2 nanosheets [89, 95]. When flower-like Mn-doped MoS_2 is exposed to visible light irradiation, the absorption band around 600 nm for pure MoS_2 gradually shifted towards higher wavelengths with increasing the doping ratio, causing edge position redshift. This shift enhances visible-light absorption and promotes the generation of electron–hole pairs, which can contribute to the improved photocatalytic activity of the Mn-doped samples [44]. This behavior which can be attributed to quantum confinement and edge effects, is a good indication that substituted Mn-doped MoS_2 has more absorption ability than the pure one

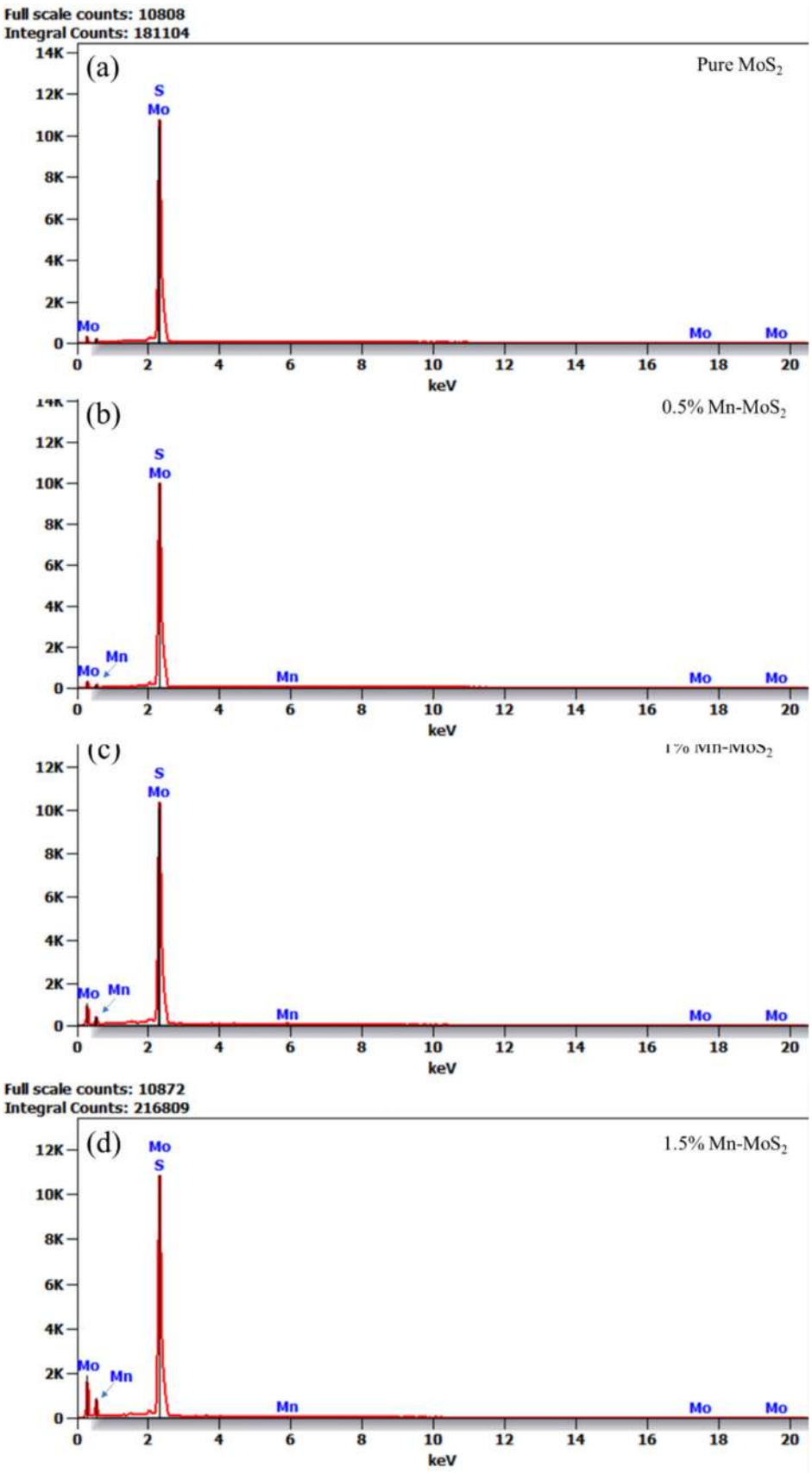

Fig. 9 EDX spectra of $Mo_{1-x}Mn_xS_2$ NFs **(a)** pure MoS_2, **(b)** x = 0.005, **(c)** x = 0.01, and **(d)** x = 0.015

Table 2 Elemental composition (atomic %) of pure and Mn-doped $Mo_{1-x}Mn_xS_2$ nanoflowers determined by EDX spectroscopy

Sample	Atomic %		
	Mo	S	Mn
Pure MoS_2	34.2	65.8	0
$Mo_{0.995}Mn_{0.005}S_2$	29.9	69.8	0.3
$Mo_{0.99}Mn_{0.01}S_2$	34.3	64.9	0.8
$Mo_{0.985}Mn_{0.015}S_2$	37.7	60.9	1.4

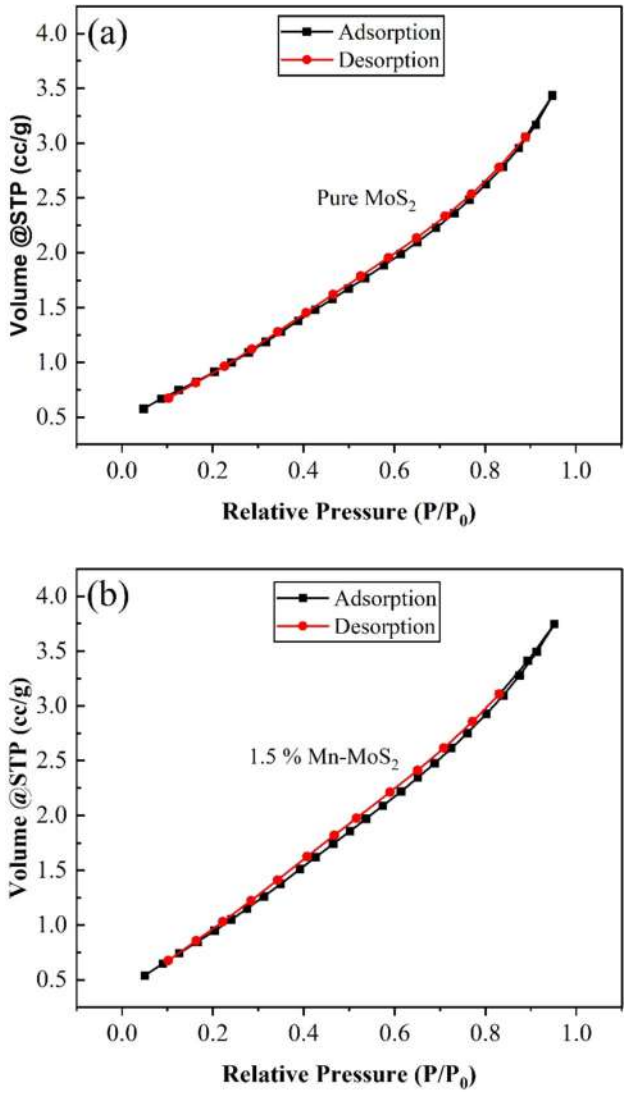

Fig. 10 N_2 adsorption–desorption isotherms of **(a)** pure and **(b)** 1.5% Mn-doped MoS_2

[96, 97]. The few-layered hybrid structure of MoS_2 prepared by the hydrothermal technique reflects why MoS_2 has a prominent absorption peak rather than a sharp one in the UV–Vis zone [98].

Table 3 BET specific surface area of the $Mo_{1-x}Mn_xS_2$ nanoflowers

Sample	Specific surface area (cm^2/g)
Pure MoS_2	196,800
$Mo_{0.995}Mn_{0.005}S_2$	234,000
$Mo_{0.99}Mn_{0.01}S_2$	236,000
$Mo_{0.985}Mn_{0.015}S_2$	241,000

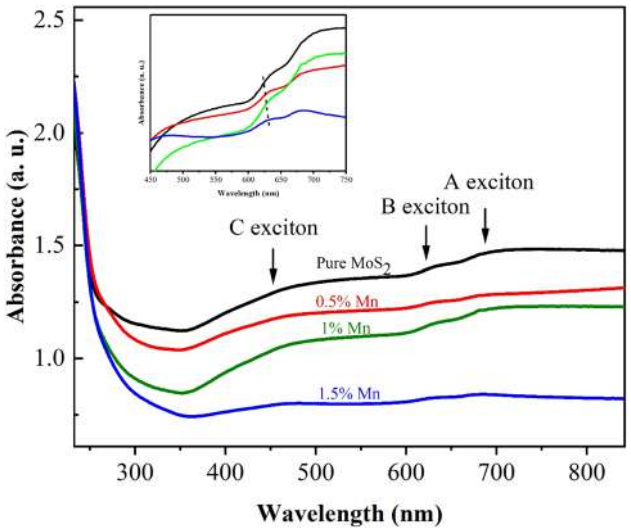

Fig. 11 UV–Vis absorption spectra of $Mo_{1-x}Mn_xS_2$ NFs

Furthermore, the energy band gaps of the synthesized $Mo_{1-x}Mn_xS_2$ ($0 \leq x \leq 0.015$) nanosystem samples were estimated using the Tauc Plot relation (Eq. 9) in terms of the calculated absorption coefficient α (Eq. 10) [99–101].

$$(\alpha h\nu) = B(h\nu - E_g)^m \tag{9}$$

$$\alpha = \frac{2.303\rho \times 10^3}{lcM} A \tag{10}$$

The average optical bandgap (E_g) for each sample was determined by plotting $(\alpha h\nu)^m$ on the Y-axis versus the photon energy (hν) on the X-axis and extrapolating the linear region of the curve to the X-axis (i.e., $(\alpha h\nu)^m = 0$). Where h is Planck's constant, ν is the photon frequency, m is the exponent that may equal 1/2, 2 and 1/3, 3 for direct, indirect allowed transition, and direct, indirect forbidden transition, respectively, B represents a constant relative to the materials and unaffected by photon energy, ρ is the theoretical density of each specimen, A is the absorbance, L is the optical path length inside the solution, c is the concentration, and M is the molecular weight.

As shown in Fig. 12, the direct bandgaps of $Mo_{1-x}Mn_xS_2$ NFs are determined to be 1.88 eV, 1.78 eV, and 1.7 eV for $x = 0.005$, $x = 0.01$, and $x = 0.015$,

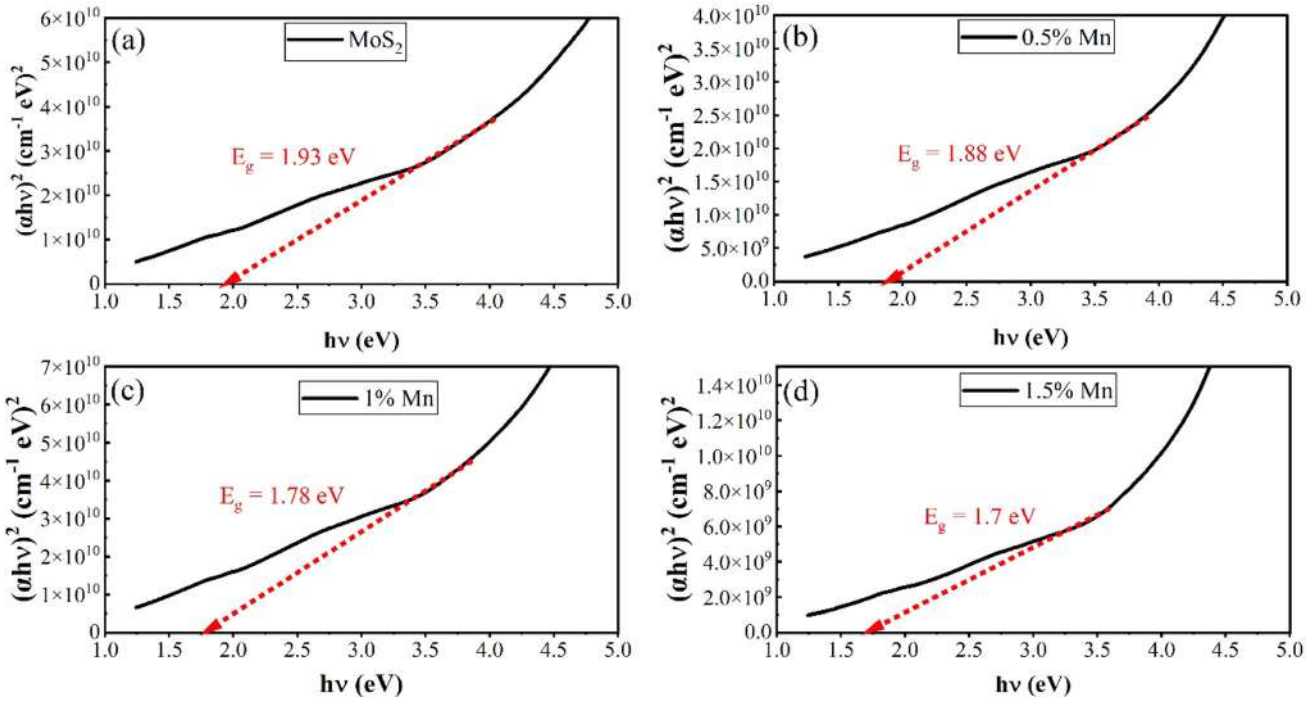

Fig. 12 Tauc-plot for direct bandgap of $Mo_{1-x}Mn_xS_2$ NFs

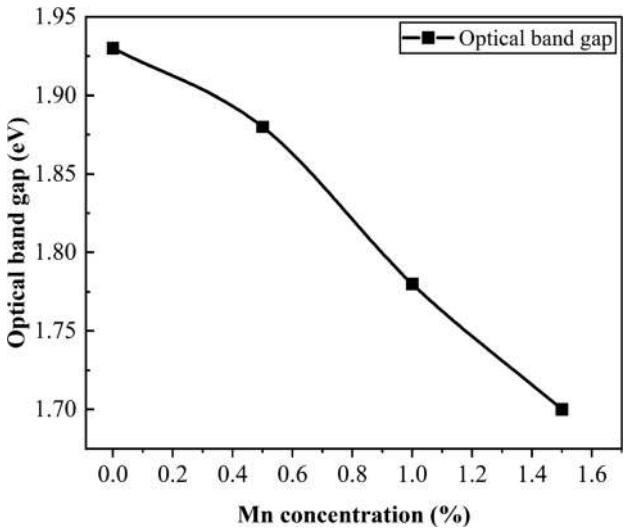

Fig. 13 Change of the optical bandgap with Mn ratio of $Mo_{1-x}Mn_xS_2$ ($0 \leq x \leq 0.015$) NFs

respectively, which are lower than that of pure MoS_2 ($E_g = 1.93$ eV). Figure 13 further demonstrates that a gradual reduction in the optical bandgap by 0.23 eV has been accomplished for 1.5% Mn-doped MoS_2. This reduction, which is compatible with previous theoretical calculations based on density functional theory (DFT), can be explained by the introduction of Mn as a transition metal ion, which reduces the bandgap by lifting the valence band edge due to some energy levels created within the bandgap by the dopant element [44, 102]. Hence, it is expected that Mn-doped MoS_2 nanoparticles will have more effective photocatalytic performance than pure MoS_2.

4.8. Photocatalytic studies

4.8.1. Methylene blue degradation

To study the photocatalytic activity of pristine and Mn-doped MoS_2 NFs, an aqueous solution of MB dye photodegradation was evaluated under visible light irradiation ($\lambda > 420$ nm) at room temperature in the presence of the synthesized $Mo_{1-x}Mn_xS_2$ ($0 \leq x \leq 0.015$) NFs. The degradation of MB molecules was followed up by monitoring the gradual decrease of the characteristic peak, which is centered at 664 nm in the time-dependent absorption spectra of MB, detected by a UV–Vis spectrophotometer [103]. As shown in Fig. 14a, there is no noticeable decrease with time in the maximum absorbance intensity, which means that the photolysis of MB dye in the absence of a photocatalyst is negligible and the degradation process relies entirely on the presence of the photocatalyst. In contrast, when $Mo_{1-x}Mn_xS_2$ (from $x = 0$ to $x = 0.015$) powder samples were used as photocatalysts, a relatively rapid and consistent reduction in MB concentration was observed with increasing irradiation time from 0 to 60 min, as shown in Fig. 14b–e.The efficiency (E%) of dye degradation was calculated via Eq. (11) [104].

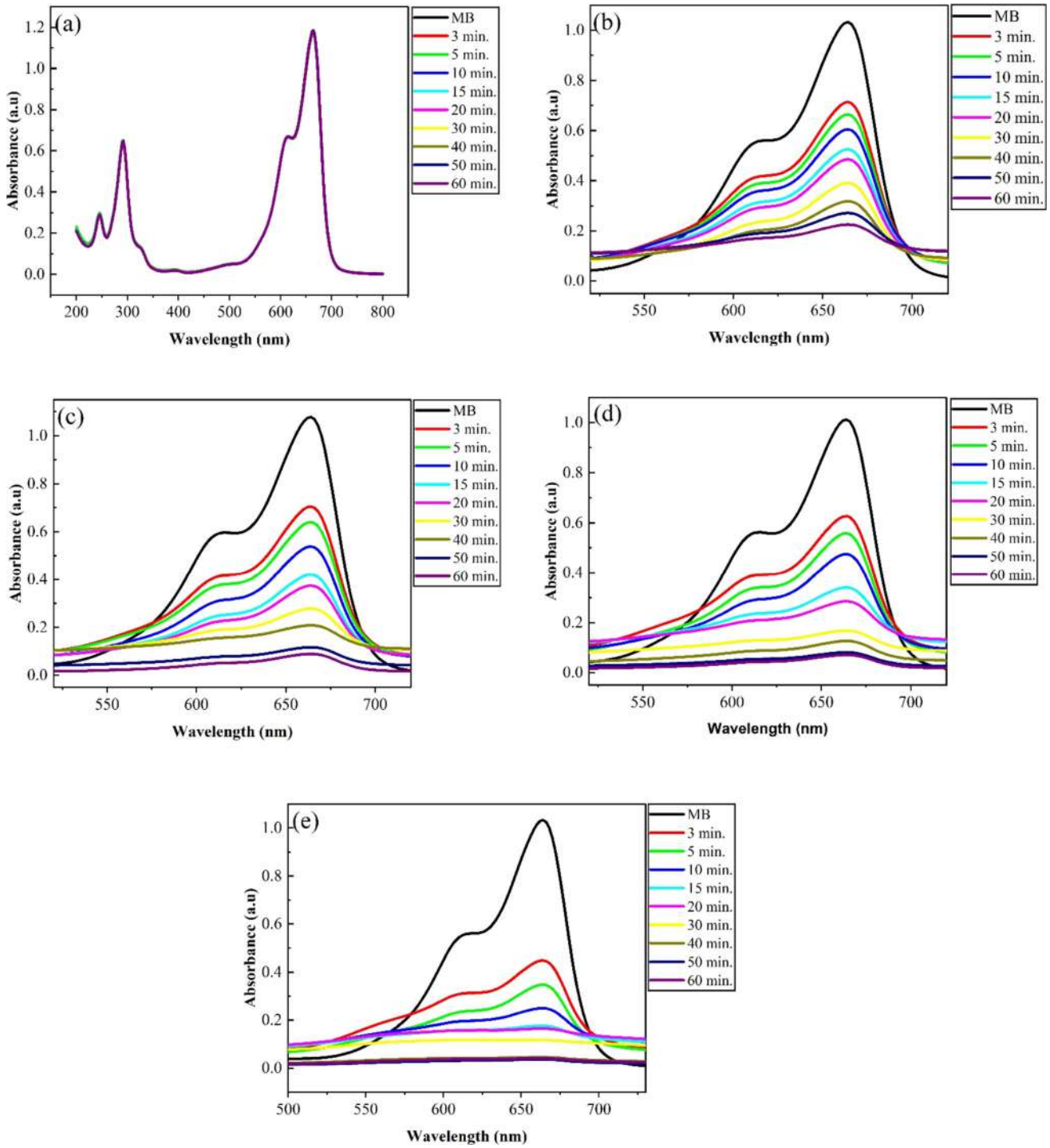

Fig. 14 UV–visible spectra measured at different time intervals of MB degradation under visible light exposure in the presence of: **(a)** MB dye (control), **(b)** pristine MoS_2, **(c)** 0.5% Mn-doped MoS_2, **(d)** 1% Mn-doped MoS_2, and **(e)** 1.5% Mn-doped MoS_2

$$E\% = \frac{A_0 - A_t}{A_0} \times 100 = \frac{C_0 - C_t}{C_0} \times 100 \quad (11)$$

where A_0 and A_t are the absorbance recorded at λ_{max} at 0 min and at irradiation time t, respectively, while C_0 and C_t represent the initial and final dye concentrations, respectively. The obtained results reveal that the calculated degradation percentage using pristine MoS_2 photocatalyst has the lowest dye removal percentage (E = 78%) within 60 min, which can be attributed to its limited absorbance in the visible region of electromagnetic radiation. For Mn-doped MoS_2 photocatalysts, it was found that the

degradation process became more effective and enhanced to 91.7%, 93%, and 96% for 0.5%, 1%, and 1.5% Mn-doped MoS_2, respectively. The doped samples have a higher degradation percentage when compared to the pure ones, which is a direct indication that the photocatalytic activity has been enhanced gradually by increasing the Mn concentration. This enhancement can be mainly attributed to the progressive reduction in the optical bandgap from 1.93 eV for pure MoS_2 to 1.7 eV for 1.5% Mn-doped MoS_2 [105]. Also, the doping process boosts the number of active sites of MoS_2 by controlling its morphology and suppresses electron–hole pair recombination [43, 106].

The enhanced removal efficiency with 1.5% Mn doping is attributed to the increased presence of Mn atoms that promote MB adsorption onto the MoS_2 surface, potentially resulting in the formation of additional active sites on the catalyst surface. Nevertheless, further investigations involving different organic pollutants are still required to comprehensively evaluate the effectiveness and applicability of Mn-doped MoS_2 photocatalysts toward the removal of various environmental contaminants.

To further examine the photocatalytic performance of MoS_2 and the impact of Mn doping on its photocatalytic activity rate, the relative absorbance C_t/C_0 versus time was plotted as shown in Fig. 15a for blank MB solution and $Mo_{1-x}Mn_xS_2$ ($0 \leq x \leq 0.015$) photocatalysts, where x = 0 for pure MoS_2 (control sample). The C_t/C_0 calculated ratios during the period of light irradiation are listed in Table 4. It is clear from the tabulated data that the synthesized Mn-doped MoS_2 nanoparticles are more effective for MB degradation than the pure ones. Moreover, to explore the kinetic reaction of MB photocatalytic degradation by the understudied prepared materials. The Langmuir–Hinshelwood (L–H) model, which is considered a pseudo-first-order model, was employed for the estimation of the degradation rate constant (κ) from Eq. (12) that can easily be converted to Eq. (13) through the application of the Ln function for both sides [45].

$$C_t = C_0\, e^{-\kappa t} \tag{12}$$

$$\ln\left(\frac{C_0}{C_t}\right) = \kappa t \tag{13}$$

As shown in Fig. 15b, the estimated recombination rate constant for pure MoS_2 was found to be 0.022 min^{-1} and gradually increased with increasing the Mn-dopant ratio reaching 0.051 min^{-1} for 1.5% Mn-doped MoS_2. The recombination rate constants for all the examined samples are tabulated in Table 4, which indicates that the Mn-doped MoS_2 has a higher κ values compared to the pure one due to their lower energy bandgaps, charge transfer, improved absorption of visible light, and reduced charge carrier recombination [107]. Notably, these results demonstrate that the rate constant of the 1.5% Mn-doped MoS_2 sample is 2.3 times greater than that of MoS_2, confirming the substantial enhancement in photocatalytic activity achieved through Mn incorporation.

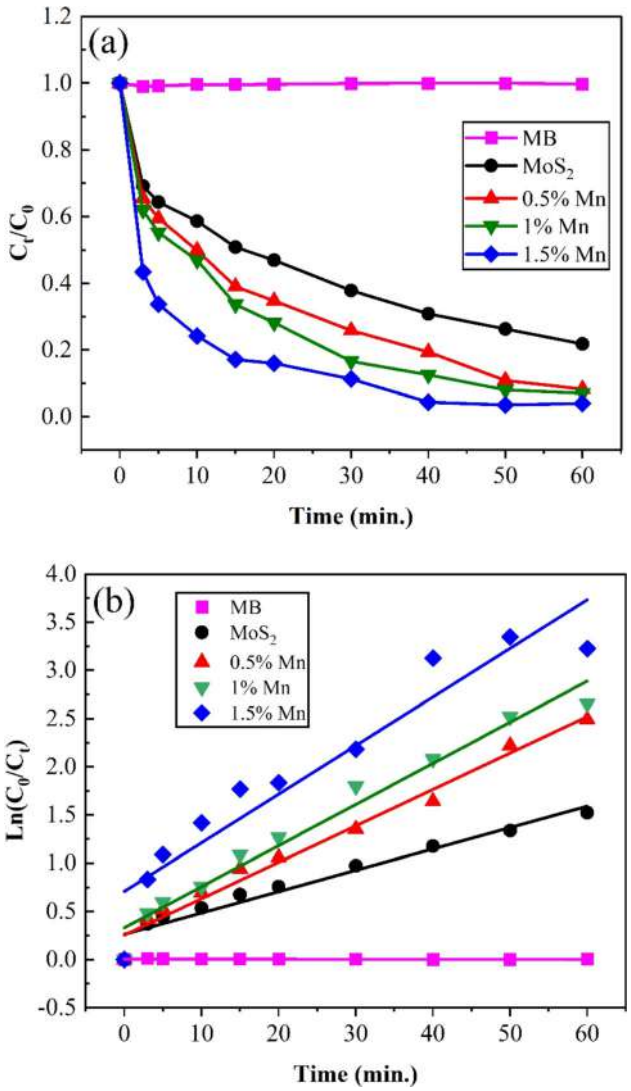

Fig. 15 **(a)** C_t/C_o plot versus duration of irradiation, **(b)** First-order kinetic decay plots of $Mo_{1-x}Mn_xS_2$ catalysts for degrading MB

Table 4 Photocatalytic degradation efficiency (E), relative absorbance (C_t/C_o), recombination rate constant (κ) and correlation coefficient (R^2) of pure and Mn-doped $Mo_{1-x}Mn_xS_2$ nanoflowers

Photocatalyst	E (%)	C_t/C_o	κ (min^{-1})	R^2
MB	0.3	0.99	-7.25×10^{-5}	–
Pure MoS_2	78	0.22	0.022	0.953
$Mo_{0.995}Mn_{0.005}S_2$	91.7	0.08	0.038	0.979
$Mo_{0.99}Mn_{0.01}S_2$	93	0.07	0.043	0.969
$Mo_{0.985}Mn_{0.015}S_2$	96	0.04	0.050	0.901

Table 5 Comparison between the photocatalytic performance of Mn-doped MoS_2-based catalysts reported in previous studies and the present work

Photocatalyst	Dye	Catalyst mass (mg)	Light source	Irradiation period (min.)	Degradation efficiency (%)	Refs.
MoS_2 nanoflowers	MB	30	25 W Murphy LED	180	91	[108]
MoS_2 nanosheets	MB	5	22 W B22 LED bulb	720	85	[109]
MoS_2 multi-wall nanotubes	RhB	10	50 W mercury lamp	60	98	[110]
MoS_2 nanoflowers	MB	20	Sun light	20	99.3	[8]
MoS_2 nanostructures	MB	20	25 W Murphy lamp	150	89.87	[59]
5% Ni-doped MoS_2	MB & RhB	10	500 W Hg lamp	240	96	[42]
5% Cd-MoS_2	MB & RhB	10	visible light	180	94	[44]
3%Ag-MoS_2	MB & RhB	10	500 W Hg lamp	230	69	[43]
20% Mn-MoS_2	MB	20	25 W Murphy lamp	90	100	[59]
N-doped MoS_2	RhB	20	175 W halogen lamp	70	99	[111]
3% Mn-MoS_2	RhB	100	compact light (60 W–220V)	240	40.9	[58]
3% Mn-MoS_2	MB	10	150 W Hg lamp	55	91	[45]
MoS_2 NFs	MB	10	150 W halogen lamp	60	78	This work
$Mo_{0.995}Mn_{0.005}S_2$					91.7	
$Mo_{0.99}Mn_{0.01}S_2$					93	
$Mo_{0.985}Mn_{0.015}S_2$					96	

The study presented here demonstrates that the as-prepared Mn-doped nanostructures are capable of decomposing MB dye molecules under visible-light stimulation. As shown in Table 5, the photocatalytic performance achieved in this work is competitive to that of the MoS_2-based nanostructures recently reported in the literature. Most previous studies required longer irradiation times, higher dopant concentrations, or the use of higher-intensity light sources to achieve comparable degradation efficiencies for organic pollutants.

4.8.2. Photocatalytic mechanism

The photocatalytic degradation mechanism of MB over MoS_2 under visible-light irradiation can be explained based on the reaction mechanism, band structure, and charge-transfer processes of the photocatalyst, as illustrated in Fig. 16. The positions of the conduction band (C.B) and the valence band (V.B) for MoS_2 can be computed by using Eqs. (14) and (15) [112].

$$E_{CB} = \chi - E^e - \frac{1}{2}E_g \tag{14}$$

$$E_{CB} = E_{VB} - E_g \tag{15}$$

where E_{CB} and E_{VB} represent the potential of the C.B and the V.B edge, respectively, χ refers to the semiconductor electronegativity, which is equal to 5.32 eV in the case of MoS_2, E_e is known as the energy of unbound electrons on the hydrogen scale (4.50 eV), and E_g is the energy bandgap (1.9 eV for MoS_2) [107]. Based on Eqs. (14) and (15), the values of E_{CB} and E_{VB} for pristine MoS_2 are equal to −0.13 eV and 1.77 eV, respectively. These values can be altered by introducing transition metal ions through the doping process. First, when the photocatalyst and the dye are mixed in the absence of light, they have a sufficient interaction that causes the dye molecules to attract and stick to the photocatalyst surface. Next, when the dye solution is exposed to visible light and the incident photons with energies equal to or greater than the optical bandgap of the photocatalyst, electron (e^-)–hole (h^+) pairs are generated. The generated holes in the V.B play the most important portion of MB degradation as they interact with H_2O molecules to form $OH^\bullet$ (hydroxide radical) and H^+ ions. Also, superoxide radicals $O_{2^-}^\bullet$ are formed when the oxygen that sticks to the catalyst surface reacts with the electrons in the C.B. Then H_2O_2 is produced when H^+ ions combine with the superoxide radicals $O_{2^-}^\bullet$. After that, H_2O_2

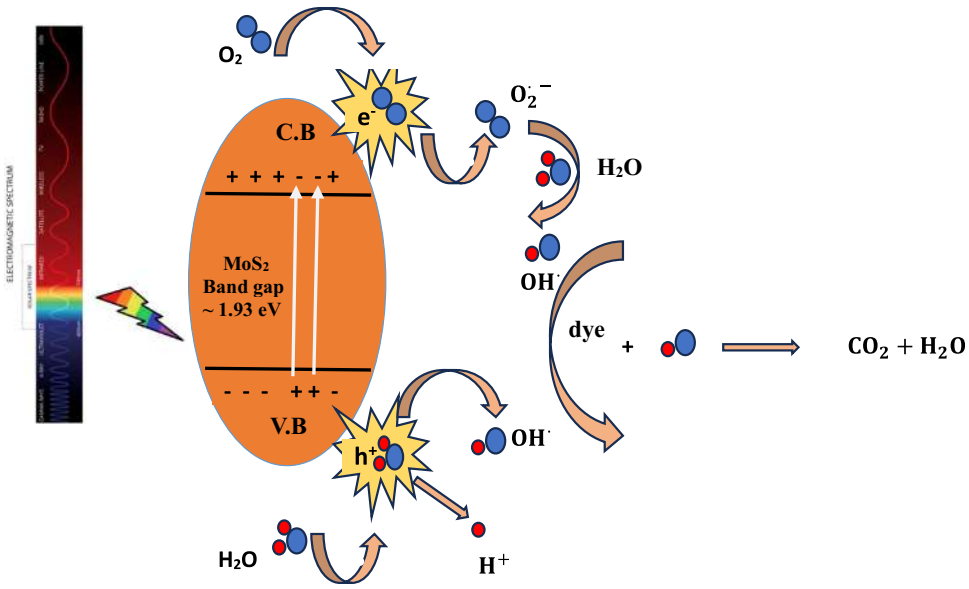

Fig. 16 Photodegradation mechanism of organic pollutants using MoS_2 photocatalyst

decomposes into hydroxyl radicals $OH^{\bullet}$ and OH^{-}. Finally, these produced hydroxyl radicals interact with the organic pollutants in MB and break down into CO_2 and H_2O [113]. Sahoo et al. investigated this photocatalytic mechanism using free radical trapping experiments with various scavenger reagents [59]. The following reactions (Eqs. 16–21) summarize how MoS_2 degrades a dye:

$$MoS_2 + \text{Visiblelight} \rightarrow MoS_2(e^- + h^+) \quad (16)$$

$$MoS_2(h^+) + H_2O \rightarrow H^+ + OH^{\bullet} \quad (17)$$

$$MoS_2(e^-) + O_2 \rightarrow O_2^{\bullet -} \quad (18)$$

$$O_2^{\bullet -} + 2H^+ + e^- \rightarrow H_2O_2 \quad (19)$$

$$H_2O_2 + e^- \rightarrow OH^{\bullet} + OH^- \quad (20)$$

$$OH^{\bullet} + Dye(\text{organic pollutants}) \rightarrow CO_2 + H_2O\,(\text{degradation products}) \quad (21)$$

5. Conclusion

$Mo_{1-x}Mn_xS_2$ NFs were successfully synthesized via a simple one-step hydrothermal method using ammonium molybdate tetrahydrate, manganese (II) acetate tetrahydrate, and thiourea as the source materials in the absence of any surfactants, from x = 0 for pure MoS_2 up to x = 0.015 in steps of 0.005 for Mn-doped MoS_2 samples. The hexagonal crystal structure of the 2H-MoS_2 polytype was confirmed to be present in all the prepared samples by XRD analysis, with no other foreign oxides or impurities detected. With increasing the substituted Mn ratio, it was found that the lattice parameters increased and the average crystallite size decreased to be in the range of 5–7 nm. SEM images verified that both pure and Mn-doped samples have flower-like microspheres consisting of 2D nanosheets, while the overall morphology remained nearly unaffected by the Mn doping process due to the relatively low dopant concentration. The characteristic vibrational modes located between 400 and 900 cm^{-1} in the FT-IR spectra were due to the characteristic vibration bands of the MoS_2 structure. The enhancement in the catalyst's surface area by increasing the Mn doping concentration is confirmed through BET surface area analysis. The proposed formation of $Mo_{1-x}Mn_xS_2$ NFs is confirmed using energy dispersive X-ray spectroscopy (EDX). UV–visible examinations implied that Mn ion doping reduced the optical bandgaps significantly from 1.93 eV for pristine MoS_2 to 1.70 eV for 1.5% Mn-doped MoS_2, which is related to the development of sub-levels between the energy bandgaps. Among all investigated samples, the 1.5% Mn-doped MoS_2 achieves a maximal photocatalytic degradation of 96% MB in 60 min. Mn doping in MoS_2 significantly improves photocatalytic activity, creating new possibilities for 2D photocatalysts.

Funding This research received no specific grant from any funding agency in the public, commercial, or not-for-profit sectors.

Declarations

Conflict of interest The authors declare no competing interests.

Consent to participate All authors accepted.

Consent for publication All authors accepted.

References

[1] D J Yang, Z F Zheng, H Y Zhu, H W Liu and X P Gao *Adv. Mater.* **20** 2777 (2008).
[2] C C Wang, J R Li, X L Lv, Y Q Zhang and G Guo *Energy Environ. Sci.* **7** 2831 (2014).
[3] R Ameta, S Benjamin, A Ameta and S C Ameta *Mater. Sci. Forum* **734** 247 (2013).
[4] K Hashimoto, H Irie and A Fujishima *Jpn. J. Appl. Phys.* **44** 8269 (2005).
[5] Q Guo, C Zhou, Z Ma and X Yang *Adv. Mater.* **31** 1901997 (2019).
[6] U G Akpan and B H Hameed *J. Hazard. Mater.* **170** 520 (2009).
[7] Y J Jang, C Simer and T Ohm *Mater. Res. Bull.* **41** 67 (2006).
[8] H Sadhanala, S Senapati, K V Harika, K K Nanda and A Gedanken *New J. Chem.* **42** 14318 (2018).
[9] M Pelaez et al *Appl. Catal. B* **125** 331 (2012).
[10] D Komaraiah, E Radha, J Sivakumar, M R Reddy and R Sayanna *Opt. Mater.* **108** 110401 (2020).
[11] F Zhang, Y H Li, J Y Li, Z R Tang and Y J Xu *Environ. Pollut.* **253** 365 (2019).
[12] S Bera, S Ghosh, T Maiyalagan and R N Basu *ACS Appl Energy Mater.* **5** 3821 (2022).
[13] D Chin, Clare, P Fontenot, T Rostamzadeh, L J Treadwell, R H. Schmehl and J B Wiley *ACS Appl. Energy Mater.* **5** 14687 (2022)
[14] H Issa Hamoud et al *J. Am. Chem. Soc.* **144** 16433 (2022).
[15] K Paul and P Giri *Plasmonic Metal and Semiconductor Nanoparticle Decorated TiO_2-Based Photocatalysts for Solar Light Driven Photocatalysis* (Elsevier) Vol 4, p 786 (2018)
[16] R Yang et al *Angew. Chem.* **135** e202218016 (2023).
[17] H Wang, H Yuan, S S Hong, Y Li and Y Cui *Chem. Soc. Rev.* **44** 2664 (2015).
[18] D Kaplan, Y Gong, K Mills, V Swaminathan, P Ajayan, S Shirodkar and E Kaxiras *2D Mater.* **3** 015005 (2016).
[19] M Pumera and A H Loo *TrAc Trends Anal. Chem.* **61** 49 (2014).
[20] H Schmidt, F Giustiniano and G Eda *Chem. Soc. Rev.* **44** 7715 (2015).
[21] N Thomas, S Mathew, K M Nair, K O'Dowd, P Forouzandeh, A Goswami, G McGranaghan and S C Pillai *Mater. Today Sustain.* **13** 100073 (2021).
[22] Z Li, X Meng and Z Zhang *J. Photochem. Photobiol. C Photochem. Rev.* **35** 39 (2018).
[23] I Song, C Park and H C Choi *RSC Adv.* **5** 7495 (2015).
[24] C Lee, H Yan, L E Brus, T F Heinz, J Hone and S Ryu *ACS Nano* **4** 2695 (2010).
[25] E Singh and K S Kim *Mater. Interfaces* **9** 3223 (2017).
[26] L Chacko, A Poyyakkara, V S Kumar and P Aneesh *Fundamentals and Properties of Multifunctional Nanomaterials* (Elsevier) Chapter 19, Section 3, p 499 (2021)
[27] E Ghaleghafi and M B Rahmani *J. Mater. Sci.* **56** 11749 (2021).
[28] K Momma and F Izumi *J. Appl. Crystallogr.* **44** 1272 (2011).
[29] M Xu, T Liang, M Shi and H Chen *Chem. Rev.* **113** 3766 (2013).
[30] Y Okuno, O Lancry, A Tempez, C Cairone, M Bosi, F Fabbri and M Chaigneau *Nanoscale* **10** 14055 (2018).
[31] G Deokar, N Rajput, P Vancsó, F Ravaux, M Jouiad, D Vignaud, F Cecchet and J F Colomer *Nanoscale* **9** 277 (2017).
[32] P Nandigana, S Mahato, M Dhandapani, B Pradhan, B Subramanian and S K Panda *J. Alloys Compd.* **907** 164470 (2022).
[33] Z Li, X Meng and Z Zhang *Catal. Today* **315** 67 (2018).
[34] X Li, S Guo, W Li, X Ren, J Su, Q Song, A J Sobrido and B Wei *Nano Energy* **57** 388 (2019).
[35] C Wang, Y Zhan and Z Wang *ChemistrySelect* **3** 1713 (2018).
[36] M-J Hwang, S W Han, T B Nguyen, S C Hong and K S Ryu *J. Nanosci. Nanotechnol.* **12** 5884 (2012).
[37] Ritika, M Kaur, A Umar, S K Mehta, S Singh, S K Kansal, H Fouad and O Y Alothman *Materials* **11** 2254 (2018)
[38] R Selvaraj, K R Kalimuthu and V Kalimuthu *Lett.* **243** 183 (2019).
[39] A Ghalajkhani, M Haghighi and M Shabani *J. Photochem. Photobiol. A Chem.* **359** 145 (2018).
[40] Y Zheng, J Wang, Y Wang, H Zhou, Z Pu, Q Yang and W Huang *Molecules* **25** 2 (2019).
[41] Z Guan, P Wang, Q Li, Y Li, X Fu and J Yang *Eng. J.* **327** 397 (2017).
[42] M Khan et al *Mater. Res. Express* **7** 015061 (2020).
[43] A Nazneen, M Khan, M Naeem, M Atif and M Iqbal *J. Mol. Struct.* **1220** 128735 (2020).
[44] M Farooq and T Iqbal *J. Inorg. Organomet. Polym. Mater.* **32** 4422 (2022).
[45] S Sasi, B Beegum, C Thomas, L M Joseph, V Shinoj and R Reshmi *J. Alloys Compd.* **951** 169856 (2023).
[46] S Ishihara et al *Jpn. J. Appl. Phys.* **55** 04EJ07 (2016).
[47] X Wang, H Feng, Y Wu and L Jiao *J. Am. Chem. Soc.* **135** 5304 (2013).
[48] A S George et al *Adv. Funct. Mater.* **24** 7461 (2014).
[49] S E Skrabalak and K S Suslick *J. Am. Chem. Soc.* **127** 9990 (2005).
[50] S Qin, W Lei, D Liu and Y Chen *Rep.* **4** 7582 (2014).
[51] H A Therese, N Zink, U Kolb and W Tremel *Solid State sci.* **8** 1133 (2006).
[52] N Li, Y Chai, Y Li, Z Tang, B Dong, Y Liu and C Liu *Mater. Lett.* **66** 236 (2012).
[53] N Chaudhary *Actuators A Phys.* **277** 190 (2018).
[54] S A Darsara, M Seifi and M B Askari *Optik* **169** 249 (2018).
[55] B Pourabbas and B Jamshidi *Chem. Eng. J.* **138** 55 (2008).
[56] G Wang, Z Wang, Y Zhang, G Fei and L Zhang *Nanotechnology* **15** 1307 (2004).
[57] H Hu, X Huang, C Deng, X Chen and Y Qian *Chem. Phys.* **106** 58 (2007).
[58] P T T Trang, T C Duc, T T Tam, V Vien and N H Lien *J. Catal. Adsorpt.* **9** 119 (2020).
[59] D Sahoo, S Tyagi, S Agarwal, J Shakya, N Ali, W J Yoo and B Kaviraj *Langmuir* **39** 7109 (2023).
[60] S S Singha, S Rudra, S Mondal, M Pradhan, A K Nayak, B Satpati, P Pal, K Das and A Singha *Electrochim. Acta* **338** 135815 (2020).
[61] L Lin, J Huang, W Yu, L Zhu, H Tao, P Wang and Y Guo *Solid State Commun.* **301** 113702 (2019).
[62] Y T Gaim, S M Yimanuh and Z G Kidanu *J. Composit. Sci.* **6** 317 (2022).
[63] M Chen, X Jian, H Wu, J Huang, W Liu and Y Liu *Nanotechnology* **31** 205403 (2020).
[64] P Sharma, M K Singh and M S Mehata *J. Mol. Struct.* **1249** 131651 (2022).
[65] M K Singh, P Chettri, A Tripathi, A Tiwari, B Mukherjee and R Mandal *Chem. Chem. Phys.* **20** 15817 (2018).
[66] H Song, A Tang, G Xu, L Liu and Y Pan *J. Electrochem. Sci.* **13** 6708 (2018).
[67] S Wang, Z Wang, J Qin, W Wang, W Li and D He *Chem. Phys.* **130** 170 (2011).
[68] R Sanikop, S Gautam, K H Chae and C Sudakar *J. Magn. Magn. Mater.* **537** 168226 (2021).
[69] D Nath, F Singh and R Das *Chem. Phys.* **239** 122021 (2020).
[70] Available from: http://mill2.chem.ucl.ac.uk/tutorial/lmgp/celref.htm
[71] A El-Fadl, M Hussien, A Soltan and A Abu-Sehly *Dig. J. Nanomater. Bios.* **19** (2024)
[72] Q Xiong, X Zhang, H Wang, G Liu and G Wang *Commun.* **54** 3859 (2018).

[73] L Luo, M Shi, S Zhao, W Tan and X Lin *J. Saudi Chem. Soc.* **23** 762 (2019).
[74] Y Yao, K Ao, P Lv and Q Wei *Nanomaterials* **9** 844 (2019).
[75] J Wang, F Sun, S Yang, Y Li, C Zhao, M Xu, Y Zhang and H Zeng *Appl. Phys. Lett.* **109** 092401 (2016).
[76] M R Gao *Commun.* **6** 7493 (2015).
[77] D Kong, H Wang, J J Cha, M Pasta, K J Koski, J Yoa and Y Cui *Nano Lett.* **13** 1341 (2013).
[78] H Wang, Z Lu, D Kong, J Sun, T M Hymel and Y Cui *ACS nano* **8** 4940 (2014).
[79] W Wang et al *Adv. Funct. Mater.* **29** 1901958 (2019).
[80] D Mosconi, P Till, L Calvillo, T Kosmala, D Garoli, D Debellis, A Martucci, S Agnoli and G Granozzi *Surfaces* **2** 531 (2019).
[81] L Chacko, P K Rastogi, T N Narayanan, M Jayaraj and P Aneesh *RSC Adv.* **9** 13465 (2019).
[82] Q Lu, Z Wei, J Liang, C Li, L Li and J Ma *ChemistrySelect* **7** e202102794 (2022).
[83] Q Zhu, H Zhang, Y Li, H Tang and J Zhou *J. Mater. Sci.* **57** 8100 (2022).
[84] A Barreto et al *J. Nanopart. Res.* **13** 6545 (2011).
[85] A Kumari, S K Yadav, Y B Pakade, B Singh and S C Yadav *B Biointerfaces* **80** 184–192 (2010).
[86] Y Zhang, P Chen, F Wen, C Huang and H Wang *Ionics* **22** 1095 (2016).
[87] M Mahdavi, S Kimiagar and F Abrinaei *Cryst.* **10** 164 (2020).
[88] S P Vattikuti and C Byon *J. Nanomater.* **2015** 9 (2015).
[89] R Rahman, D Samanta, A Pathak and T K Nath *RSC Adv.* **11** 1303 (2021).
[90] B Qi, X He, G Zeng, Y Pan, G Li, G Liu, Y Zhang, W Chen and Y Sun *Nat. Commun.* **8** 825 (2017).
[91] M Mahmoodabadi, M T Goodarzi, N Salehi, A Jalali and E Zahedi *Sci. Rep.* **15** 22788 (2025).
[92] X Feng, R Long, C Liu and X Liu *Purif. Technol.* **302** 122138 (2022).
[93] J Zolgharnein and M Rastgordani *J. Chemom.* **32** e3043 (2018).
[94] P Falcaro et al *Adv. Mater.* **23** 3901 (2011).
[95] J Y Wu, M N Lin, L D Wang and T Zhang *J. Nanomater.* **2014** 107 (2014).
[96] B Li et al *Sci. Rep.* **7** 11182 (2017).
[97] H Peng, J Lu, C Wu, Z Yang, H Chen and W Song *Surf. Sci.* **353** 1003 (2015).
[98] M Zhou, L Cheng, Z Chen and Y Ma *J. Alloys Compd.* **869** 159322 (2021).
[99] B D Viezbicke, S Patel, B E Davis and D P Birnie III *Phys. Status Solidi B* **252** 1700 (2015).
[100]T Cassagneau, J H Fendler and T E Mallouk *Langmuir* **16** 241 (2000).
[101]A A El-Fadl and A S Soltan *Uni. Sci. J.* **53** 308 (2024).
[102]A Ramasubramaniam and D Naveh *Phys. Rev. B* **87** 195201 (2013).
[103]I Khan et al *Water* **14** 242 (2022).
[104]L Chen, J Li and Q Cai *Surf. Sci.* **273** 82 (2013).
[105]A A El-Fadl, A M Hassan and M A Kassem *arXiv preprint* arXiv:2012.14232 (2020)
[106]D P Kumar, M I Song, S Hong, E H Kim and M Gopannagari *Chem. Eng.* **5** 7651 (2017).
[107]S Asaithambi, P Sakthivel, M Karuppaiah, K Balamurugan, R Yuvakkumar, M Thambidurai and G Ravi *J. Alloys Compd.* **853** 157060 (2021).
[108]D Sahoo, J Shakya, N Ali, W J Yoo and B Kaviraj *Langmuir* **38** 1578 (2022).
[109]D Sahoo, B Kumar, J Sinha, S Ghosh, S S Roy and B Kaviraj *Rep.* **10** 10759 (2020).
[110]S P Vattikuti, C Byon and C V Reddy *Superlattices Microstruct.* **85** 124 (2015).
[111]P Liu, Y Liu, W Ye, J Ma and D Gao *Nanotechnology* **27** 225403 (2016).
[112]M Yan, Y Wu, F Zhu, Y Hua and W Shi *Phys. Chem. Chem. Phys.* **18** 3308 (2016).
[113]K Lalithambika, K Shanmugapriya and S Sriram *Appl. Phys. A* **125** 1 (2019).